

Mechanical Intelligence in Propulsion via Flexible Caudal Fins

Sushrut Kumar^a, Matthew J. McHenry^b, Jung-Hee Seo^a, and Rajat Mittal^a

This manuscript was compiled on April 1, 2025

Fish swim with flexible fins that stand in stark contrast to the rigid propulsors of engineered vehicles, though it is unclear whether this flexibility endows animals with a performance advantage. Using numerical simulations of the mechanics of flow-structure interaction (FSI), we found that flexible fins are up to 70% more efficient than rigid fins. By comparing the dynamics of FSI, we find that the power requirements of rigid fins can be largely attributed to their propensity to generate high-magnitude lateral forces. In contrast, flexible fins achieve high efficiency by a mechanism known as local-force redirection where deformations orient fluid forces in fore-aft and dorso-ventral directions to reduce the power demand of generating lateral forces. These deformations occur at moments in the tail-beat cycle when large velocities and pressure differentials are generated due to the mechanics of the fin and surrounding flow. In this way, high flexibility of a caudal fin offers a form of mechanical intelligence for efficient locomotion without the sensing and computational control that might otherwise be provided by the nervous system of a fish or a computer within a submersible. Therefore, passive flow-structure interactions are critical to the performance of fish swimming and offer insight into bioinspired flexible propulsion in robotics and other engineering applications.

Swimming | Mechanical Intelligence | Propulsion | Fluid-Structure Interaction |

Nature excels at utilizing soft materials and structures that bend, deform, and stretch as they interact with the environment. In contrast to the ‘robotic’ motion of engineered systems, animal locomotion is characterized by fluid movement that is largely facilitated by passive mechanical properties. Examples include the wing deformation of flying insects and birds (1–3), the stability enhancement provided by limb deformation in insects (4, 5) and the muscle-tendon compliance of vertebrates (6, 7). These passive mechanical properties endow animals with a rapid and robust capacity to respond to perturbations. By facilitating smooth and stable motion with passive mechanics, less sensing, control and computation may be required to control these dynamic systems. This capacity to offload computation for passive mechanics in a dynamic system is known as “mechanical intelligence” and it offers inspiration for the design of a variety of robots and other devices (8–11). However, it is largely unclear to what extent passive mechanical properties enhance the energetic efficiency of biological and engineered systems.

Swimming offers a compelling system to test the efficiency gains from mechanical intelligence in animals. The passive mechanics of a swimmer’s body and fins deform as a consequence of their coupled mechanical interactions with the surrounding water. This flow-structure interaction (FSI) is widely appreciated to play a major role in the dynamics of swimming animals such as fish, cetaceans, and pinnipeds. These animals use body and appendage (i.e., a fin, flipper, or fluke) deformation to propel themselves through water (12, 13). For example, FSI dynamics enable the body of trout to swim in a wake with minimal muscle activity to realize an energetic benefit (14, 15). Under these conditions, it is even possible for the body of a *dead* fish to swim momentarily by undulating through a turbulent wake (16, 17). Despite broad appreciation for the role of FSI in swimming, the mechanisms of efficiency gains remain mysterious.

The current study explores propulsion with numerical modeling of fish swimming. We focus on the caudal fin, which is the primary organ for thrust generation in a diversity of species (18, 19). Caudal fins are highly flexible membrane-like structures strengthened by slender bony rays that extend from the point-of-attachment on the peduncle to the tips of the fins (20, 21). In many fishes, the dorsal and ventral regions of the caudal fin have a higher density of rays (20, 21) and flexor muscles preferentially attach and actuate the dorsal and ventral margins of the caudal fin (22). In contrast, the central part of the fin has a lower density of rays and is therefore more flexible. As the fin is actuated at the dorsal

Significance Statement

Numerical simulations of the mechanical interactions between a fish-like caudal fin and the surrounding water demonstrate that the efficiency of propulsion is enhanced by high fin flexibility. By articulating the flow-structure interactions that naturally align hydrodynamic pressure forces with fin motion, this work demonstrates how performance gains may be achieved without a need for computation-intensive forms of active control. In contrast to rigid propulsors in engineered systems, fish exploit passive material properties to direct mechanical work away from power-consumptive lateral force and towards the generation of thrust. This form of mechanical intelligence provides a foundation for bioinspired design that could improve efficiency in underwater robotics and engineered aquatic systems. Understanding how biological structures passively harness hydrodynamic forces may lead to more adaptable, energy-efficient propulsion technologies across a range of applications.

Author affiliations: ^aDepartment of Mechanical Engineering, Johns Hopkins University; ^bDepartment of Ecology and Evolutionary Biology, University of California, Irvine

Please provide details of author contributions here.

Please declare any competing interests here.

¹A.O.(Author One) contributed equally to this work with A.T. (Author Two) (remove if not applicable).

²To whom correspondence should be addressed. E-mail: author.twoemail.com

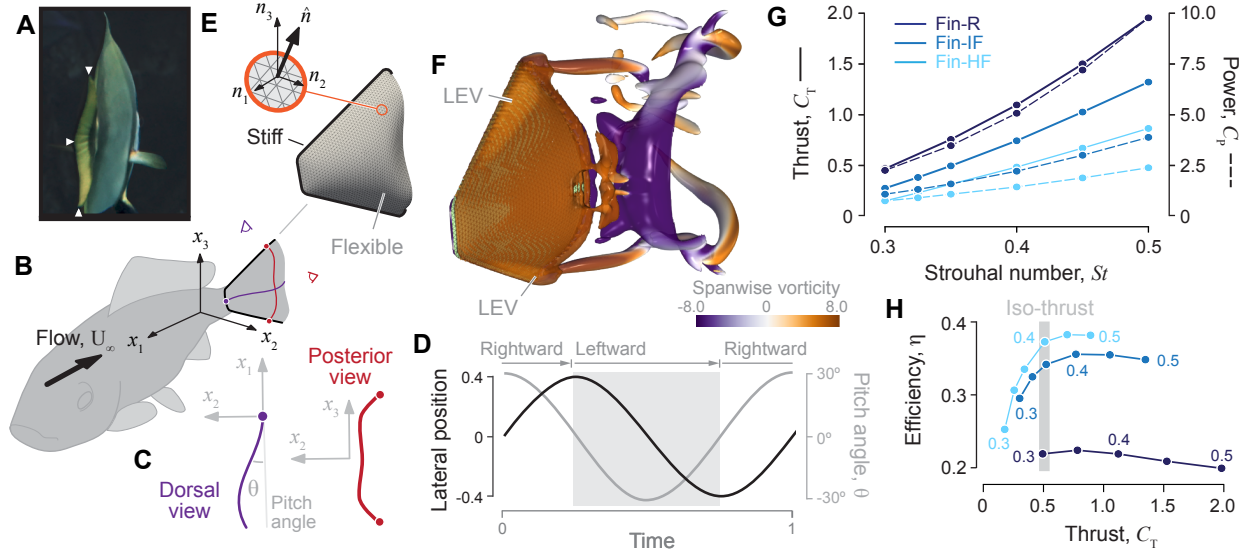


Fig. 1. Modeling the flow-structure interactions of caudal fins. (A) Video recording of a batfish (*Platax orbicularis*) from a posterior view shows how the mid-chord of the fin bends (right arrow) relative to the dorsal (down arrow) and ventral (up arrow) margins of the caudal fin as it beats toward the right. (B) Our model of the caudal fin operates in a Cartesian coordinate system (with axes x_1 , x_2 , and x_3) with deflections that may be observed along (C) the mid-chord (blue curve) in 2D from a dorsal view and along a dorso-ventral span (red curve) from a posterior view. (D) Model fins are actuated at the leading margin (at the caudal peduncle) of the fin with sinusoidal changes in lateral position (along x_2 , in black) and in pitch angle (gray curve) over normalized time (t/T , where T is the tail-beat period). (E) The FSI model included an elastic mesh between rigid dorsal and ventral margins (black curves), with deflections determined by the material stiffness and fluid forces. The inset shows a detail of the mesh, with the normal direction (\hat{n}) of a single triangle highlighted, with its components (n_1 , n_2 , and n_3) shown within the coordinate system. (F) An example simulation shows the predicted flow field (isosurfaces of the spanwise vorticity, which identifies coherent vortices by comparing the local rotation, here $Q = 5$ colored by $\omega_3 C/U_\infty$). The leading-edge vortex (LEV) is highlighted along the dorsal and ventral margins. The average (G) thrust coefficient (solid curves), power coefficient (dashed curves), and (H) efficiency are shown for simulations performed at varying Strouhal numbers (values shown for $St = 0.3, 0.4$, and 0.5). A selection of simulations at comparable C_T values were selected for 'iso-thrust' comparison (gray bar).

and ventral regions, its central area lags behind due to inertial and FSI effects and this results in a dorso-ventral curvature or “billowing” of the fin (20).

Classic studies of fish swimming identified the billowing in the caudal fin and suggested possible propulsive benefits. Bainbridge hypothesized that this dorso-ventral deformation helps smoothen out time-variation of thrust, based on films of the dace (*Leuciscus leuciscus*) (20). This deformation has been observed in other teleost species with homocercal (i.e. symmetrical) caudal fins, including the bluegill sunfish (22), mackerel (23), and batfish (Fig. 1A). However, Bainbridge’s ideas remain untested because kinematics alone do not permit an interrogation of the FSI dynamics that generate dorso-ventral deformation. Previous simulation-based studies of caudal fin hydrodynamics have either focused on *antero-posterior* deformation (24) or *imposed* dorso-ventral deformation on the fin (25). Thus, the effect of FSI-driven dorso-ventral deformation on the propulsive performance of caudal fins remains unexamined.

In the present study, we use FSI simulations to investigate the propulsive performance of a canonical model of a flexible membranous homocercal caudal fin (Fig. 1B–F). This fin is actuated with a flapping motion at the dorsal and ventral margins, but is allowed to deform passively in the central region as a consequence of fluid forces and the flexibility of the fin (details in Materials and Methods). We examine the stiffness of the central region influences thrust generation and power expenditure. This is achieved by modeling the caudal fin with three levels of flexibility. Fins of intermediate (Fin-IF) and high flexibility (Fin-HF) are constructed with the same elastic material, but respectively with intermediate

($h^* = 0.04$, where h^* is the ratio of thickness to chord length) and thin ($h^* = 0.02$) membranes. These compliant fins are compared against a perfectly rigid fin (Fin-R) that permits no material compliance. Our comparisons quantify the degree to which passive deformation in response to flow-structure interaction modifies the propulsive performance and energetic costs of fin motion.

Propulsive Efficiency

We performed a series of FSI simulations over a range of Strouhal numbers ($0.3 \leq St \leq 0.5$) to evaluate fin performance. The Strouhal number ($St = 2A_o f/U_\infty$, where f is fin flapping frequency, $2A_o$ is the peak-to-peak fin amplitude, and U_∞ is the swimming speed) indicates the average velocity of a fin relative to oncoming flow. The range of Strouhal numbers considered spans the domain where a variety of swimmers and fliers have been shown to operate during steady swimming and flying (26–28). Consistent with physical and analytical models of hydrofoils (26, 29), the coefficient of non-dimensional thrust and its power requirements increase with the Strouhal number in our FSI simulations (Fig. 1G). The increase in thrust ($\bar{C}_T = \bar{T}/(0.5\rho U_\infty^2 S_{\text{fin}})$, where ρ is water density, U_∞ is flow speed, T is thrust and S_{fin} is the area of the fin) reflects the greater momentum that the foil imparts to the fluid as it increases its frequency and/or amplitude at higher Strouhal numbers. However, the power required to generate that thrust ($\bar{C}_P = \bar{P}/(0.5\rho U_\infty^3 S_{\text{fin}})$, where P is power) varies at a different rate (Fig. 1G), which has implications for the efficiency of propulsion ($\eta = \bar{T}U_\infty/\bar{P}$).

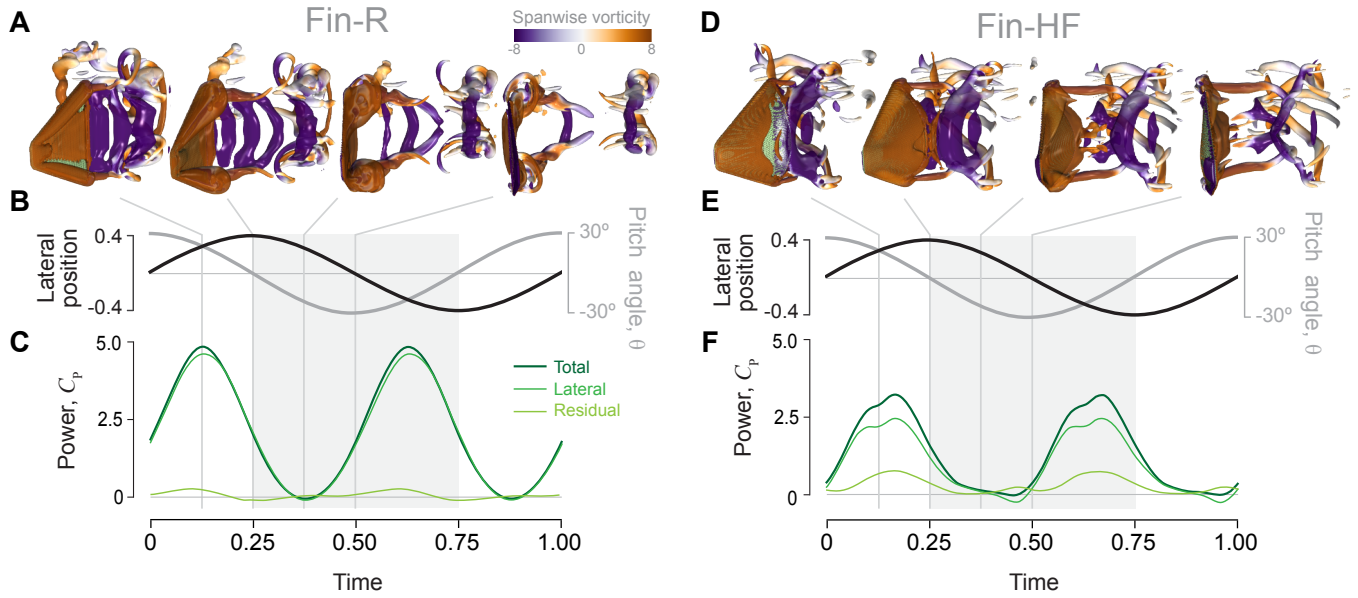


Fig. 2. The effects the contribution of lateral forces on the power requirements for propulsion in a rigid fin (Fin-R, A–C) and the most flexible fin (Fin-HF, D–F). (A) The predicted flow field (isosurfaces of the spanwise vorticity, which identifies coherent vortices by comparing the local rotation, here $Q = 5$ colored by $\omega_3 C/U_\infty$) for the rigid fin, as it is actuated with (B) oscillatory changes in lateral position (black) and pitch angle (gray), with a leftward half tail-beat (light gray) highlighted. (C) The resulting total power requirements (dark green) may be parsed with respect to the contribution to lateral forces (medium green) and the residual that expresses all remaining sources of power (light green). (D–F) The same results are shown for the flexible fin.

The thrust and the power requirements among fins of different flexibility yield contrasting trends in propulsive efficiency. The maximum efficiency of the intermediate fin (Fin-IF) is 58% greater than that of the rigid fin (Fin-R), which is exceeded by the 70% advantage of the most flexible fin (Fin-HF, Fig. 1G). Over the entire range of Strouhal numbers examined, the rigid fin is substantially outperformed in terms of efficiency by the flexible fins and this performance increases with greater compliance. However, the maximum efficiency emerges at a similar level of thrust (at $C_T \sim 0.75$) within the performance of each fin. We therefore focus our analysis of FSI mechanisms on the individual simulations for each fin that attain close to maximum efficiency, which occur at similar values of thrust ($C_T \sim 0.50$, Fig. 1H). Within this ‘iso-thrust’ comparison, the efficiency of different fins may be understood by focusing on the power requirements to actuate each fin.

The power expended by the fin to generate thrust is primarily due to the work done against the pressure-induced hydrodynamic forces on the fin. This power may be calculated by integrating the elements across the surface of the fin mesh the product of pressure difference and velocity. This approximation may be parsed as follows:

$$P(t) = \int_{S_{\text{fin}}} (\text{Lateral force}) \times (\text{Lateral velocity}) dS + \int_{S_{\text{fin}}} (\text{Pitch moment}) \times (\text{Pitch rate}) dS. \quad [1]$$

Based on the two distinct terms on the right-hand-side of the above expression, we can identify three possible mechanisms for the reduction in the power requirements of flexible fins to increase their propulsive efficiency. The first mechanism is associated with how the pressure is distributed across the fin.

This mechanism predicts that shifts in the spatial distribution of pressure forces on the flexible fins could lead to smaller pitching moments and a consequent reduction in power (due to the second term of Eqn. 1). We refer to this mechanism here as the *pitch-moment reduction* mechanism.

The remaining mechanisms relate to the lateral-force-associated term (the first term of Eqn. 1), which is expected to be a dominant contributor to power. The *force-velocity phase mismatch* mechanism posits that power requirements are reduced because fin flexibility shifts the timing of the development of lateral force relative to the lateral velocity. Finally, the *local-force-redirection* mechanism, suggests that pressure forces on the surface of the flexible fins are redirected so as to reduce lateral forces on the fin. As per Eqn. 1, any reduction in the lateral force would tend to reduce power requirements. Such an effect could emerge from the deformation of the fin surface which could direct normal pressure forces away from the lateral direction. We now consider the relative contribution of each of these three mechanisms towards enhancing the efficiency of propulsion of the flexible fins (Fig. 1H).

The Pitch-Moment Reduction Mechanism

The high efficiency of flexible fins has the potential to be assisted by how the flow-structure interaction affects the pressure distribution along the fin. In particular, if large pressure differentials are positioned further forward (towards the peduncle), then they would tend to reduce the pitching moment on the fin. This reduced pitching moment would reduce the power requirement (Eqn. 1) for propulsion and yield a higher efficiency. Such *pitch-moment reduction* appears possible, given the qualitative differences in flow across fins of different flexibility. In particular, the rigid fin develops a spiral leading-edge vortex on the dorsal and ventral

edges (LEV, Fig. 1F) that grows rapidly during the stroke of the fin and is shed from the fin by the midpoint through a half tail-beat ($t/T = 0.25$, Fig. 2A). This fin additionally sheds several distinct vortices from the trailing-edge during each half of the flapping cycle. In contrast, the LEVs over the most flexible fin are more uniform in strength along the dorsal and ventral edges, and remain attached through each half of the flapping cycle (Fig. 2D). The flexible fin also sheds one large dorso-ventral vortex from the trailing-edge in each half of the flapping cycle and this is accompanied by a pair of tip vortices.

We evaluated the effects of these differences on the contribution of the pitching moment to the power requirements for propulsion. In particular, we decomposed the pressure distribution into a component due to the lateral force ($\int_{S_{\text{fin}}} \Delta p n_2 dS \times S_{\text{fin}}^{-1} \int_{S_{\text{fin}}} V_{\text{fin}} \cdot n_2 dS$) and the residual component. This residual component encapsulates how spatial variations in the pressure differentials, particularly pitching moments, generate power requirements. This decomposition (Fig. 2C, F) shows that the work done by the fin against the lateral hydrodynamic forces accounts for the vast majority of the power requirements for both the rigid and flexible fin. However, the proportions differ with fin flexibility. For the rigid fin, the work against the lateral force comprises about 97% of required power, whereas this is 77% in the most flexible fin. The manner in which a flexible fin maintains attached LEVs (Fig. 2D) and the other changes in the flow structures cause a greater proportion of power to be applied to work against the pitching moments. Therefore, the variation of the pressure across the fin surface of the flexible fin tends to *increase* the power expenditure and *reduce* the efficiency. This result is therefore opposite to that hypothesized by the pressure-distribution mechanism. This analysis also confirms that the work done against the lateral forces, and not the pitching moment, is indeed the dominant contributor to power. Therefore, the explanation for the higher efficiency lies with the remaining two mechanisms, which are associated with the costs of generating lateral forces.

The Force-Velocity Phase Mismatch Mechanism

The *force-velocity phase mismatch* mechanism, considers the possibility that flexible fins generate efficient propulsion by shifting the timing between propulsive forces and fin velocity. Because power emerges from the product of force and velocity (Eqn. 1), power-efficient motion could be attained by generating high force at phases in the tail-beat cycle that correspond to low fin velocity, or vice-versa. In an extreme example, zero power would be required if the lateral force and the lateral velocity were completely out of phase with each other.

Instead, the fin moves with a velocity that is nearly in phase with the pressures that generate propulsion. This can be seen in the variation of the surface-averaged pressure-differential across the fin over the flapping cycle and the speed of the fin surface, among all fins (Fig. 3B–C). In addition to showing similar timing, these two quantities show non-sinusoidal variation in the pressure differential at the points where the fin reverses direction. We have estimated the phase between the lateral force and the average lateral velocity for all three fins and this is found to be 16° , 24° and 11° for Fin-R, Fin-IF and Fin-HF, respectively. Thus, we

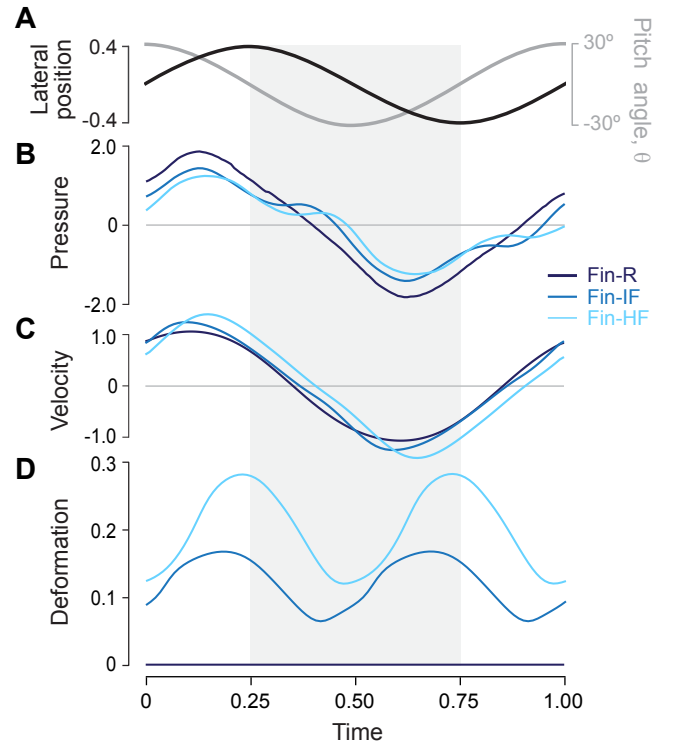


Fig. 3. Phase relationship between pressure and velocity. (A) All fins were actuated with oscillations in lateral position (black) and pitch angle (dark gray), with a leftward half tail-beat (gray field) highlighted. The resulting integrated (B) pressure differences ($1/S_{\text{fin}} \int \Delta p dS$) and (C) velocity ($1/S_{\text{fin}} \int V_{\text{fin}} dS$) of elements of the fin mesh (Fig. 1E) for fins that are rigid (Fin-R, dark blue), and of intermediate (Fin-IR, medium blue), and high (Fin-HR) flexibility. (D) Fin deformation, defined by the integrated difference in the direction of surface normals from the rigid fin ($1/S_{\text{fin}} \int (1 - \hat{n}_r \cdot \hat{n}_i) dS$).

find no consistent trends in the phase differences between force and velocity that could affect efficiency. In fact, the most flexible fin (Fin-HF), which has the highest efficiency, has a phase-difference that is *lower* than the less efficient rigid fin (Fin-R), which would tend to *increase* the power expenditure. Thus, this mechanism which is based on the phase-difference between force and velocity cannot explain the higher efficiencies of the deformable fins (Fig. 1H).

The Local-Force-Redirection Mechanism

The difference in efficiency between the fins is apparent from examination of the time course of the forces and power expenditure for each fin. Due to our iso-thrust comparison of simulations (Fig. 1H), the thrust for each fin is comparable across time (Fig. 4B). However, the lateral forces are elevated in the rigid fin compared to the flexible fins, with a maximum force that is 153% greater than the most flexible fin (Fig. 4C). Despite not assisting propulsion, these large lateral forces are key contributors to the power expenditure (Eqn. 1) and it is therefore perhaps unsurprising that the average power is up to 63% greater for the rigid fin, as compared with the most flexible fin (Fig. 4D). Therefore, having eliminated the first two mechanisms from contention, the inferior efficiency of the rigid fin may mostly be attributed to its propensity to generate larger magnitudes of energetically costly lateral forces.

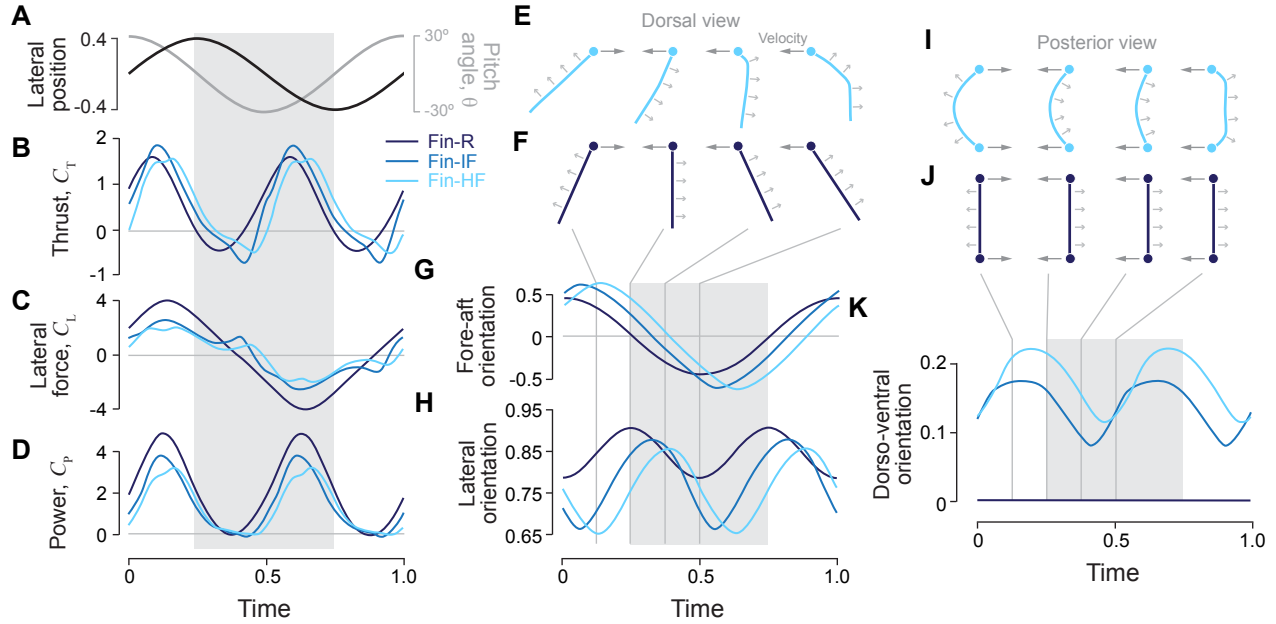


Fig. 4. Force, power, and deflection among fins at varying flexibility. (A) All fins were actuated with oscillations in lateral position (black) and pitch angle (dark gray), with a leftward half tail-beat (gray field) highlighted. The resulting coefficients of (B) thrust, (C) lateral force, and (D) power are shown for a rigid fin (Fin-R, dark blue), and fins of intermediate (Fin-IR, medium blue), and high (Fin-HR) flexibility. For the same simulations, (E–F) the deflections of the mid-chord are shown from a dorsal view (as in Fig. 1B–C) for the Fin-R (dark blue) and Fin-HF (light blue) models, with corresponding integrated fin area in the (G) fore-aft ($1/S_{\text{fin}} \int n_1 dS$) and (H) lateral ($1/S_{\text{fin}} \int n_2 dS$) orientations. (I–J) The fin deflect from a ventral view are shown for the models in E–F, with (K) corresponding integrated area of the fin in the dorso-ventral direction ($1/S_{\text{fin}} \int |n_3| dS$).

The physics associated with the generation of smaller lateral forces generated by the flexible fin may be understood by examining the dynamic changes in the fin shape (Fig. 4E–H). Bearing in mind that pressure acts perpendicular to surfaces (i.e. toward \hat{n}), we examined the orientations of the normal vectors of fin surfaces ($\hat{n} = (n_1, n_2, n_3)$) defined with respect to the coordinate system (x_1, x_2, x_3 , Fig. 1B, E) where x_1 is the direction of travel of the fish (i.e. in the direction of thrust), x_2 is the lateral direction and x_3 is the dorso-ventral direction. Integrating these components of the normal vectors across a fin’s surface provides a measure of the overall orientation of the fin and hence the potential to generate lateral force or thrust. As each fin moves through a tail-beat, the fore-aft component of its orientation sweeps through a positive (i.e. thrust-contributing) phase, followed by a negative period (i.e. drag-generating) before reversing direction (Fig. 4G). This temporal pattern is similar to the oscillations in pressure (Fig. 3B) that generate the primary forces. This pattern is similar across the fins, with a noticeably elevated orientation advantage (e.g. 27 % greater in Fin-HF than Fin-R) in the flexible fins. This is indicative of the fact that the flexible fins are more effective in orienting pressure forces towards the thrust direction than the rigid fin. However, a more dramatic difference is apparent when examining the lateral components of fin orientation (Fig. 4H). All fins oscillate in this respect, as each is pitched while being translated laterally. However, the rigid fin maintains an elevated lateral orientation throughout each tail-beat and does not exhibit the same declines exhibited as the deflected flexible fins are swept through the fluid at relatively high speed (Fig. 4E–F). Therefore, the fixed orientation of the

rigid fin contributes to the elevated lateral forces generated through a tail-beat cycle (Fig. 4C).

Another factor with respect to propulsive power is the generation of forces in the dorso-ventral direction. As a consequence of the fin deflection apparent from a posterior view (Fig. 4I), the margins of a caudal fin are tilted so as to generate a vertical component to the surface normal. The upwards and downwards components of these forces effectively cancel each other out due to their dorso-ventral symmetry. However, the sum of their absolute value is substantial (Fig. 4K) relative to the deformations that contribute to thrust (Fig. 4G). These vertical forces contribute to power reduction because they redirect and further reduce the component of the pressure force in the lateral direction (Eqn. 1). In contrast, a rigid fin presents no dorso-ventral surfaces (Fig. 4J) and hence does not exploit that direction to reduce power and enhance efficiency.

The differences in the forces over the fin are a combined effect of the force redirection mechanism associated with the fin geometry and the changes in the flow induced by fin deformation. We have devised a method to partition these effects and to parse the relative contributions of these two effects. This partitioning considers the local pressure differentials for elements of rigid (Δp_r) and flexible (Δp_f) fins, as well as the direction of the normal forces (\hat{n}_r and \hat{n}_f , respectively) from those differentials. Then, the difference of force between between the rigid and flexible fins can be expressed by the following:

$$\begin{aligned}
& \underbrace{\int_{S_{\text{fin}}} \Delta p_f \hat{n}_f dS}_{\text{Flexible fin}} - \underbrace{\int_{S_{\text{fin}}} \Delta p_r \hat{n}_r dS}_{\text{Rigid fin}} \\
&= \underbrace{\int_{S_{\text{fin}}} \Delta p_r \hat{n}' dS}_{\text{Geometry difference}} + \underbrace{\int_{S_{\text{fin}}} \Delta p' \hat{n}_r dS}_{\text{Flow difference}} \\
& \quad + \underbrace{\int_{S_{\text{fin}}} \Delta p' \hat{n}' dS}_{\text{Combined effect}}.
\end{aligned} \tag{2}$$

where $\Delta p' = \Delta p_f - \Delta p_r$ represents the difference in pressure differentials between the flexible and rigid fins, and $\hat{n}' = \hat{n}_f - \hat{n}_r$, is the change in surface inclination between the flexible and rigid fins. This equation expresses this difference in force between flexible and rigid fins in terms of the geometry only (first term), the difference due to the flow (second term), and a combined “nonlinear” effect of the two (third term).

The partitioned components of thrust offer comprehensive metrics for propulsive differences between the flexible and rigid fins. Despite generating similar thrust (Fig. 4B), the flexible fins generate lower pressure differentials (Fig. 3B) and hence negative values for the pressure difference (e.g. -0.4 in Fin-HF, Table 1). This disadvantage in pressure is more than compensated for by the difference in geometry (e.g. +0.57 in Fin-HF, Table 1). The lateral force, calculated for a half-cycle due to its zero cycle-average, reflects a power requirement that does not contribute to propulsion. The most-flexible fin generates only half the lateral force of the rigid fin, with geometry-difference and pressure-difference terms contributing similarly to this reduction (Table 1). Thus, while the pressure-difference term diminishes both the thrust and the lateral force, the geometry-difference increases thrust but decreases the lateral force. Thus, the change in fin geometry due to flexibility is clearly an important factor in the high efficiency of the flexible fins.

Fin	Forces	Flexible fin	Rigid fin	Geometry difference	Pressure difference	Combined effect
		$\int \Delta p_f n_f dA$	$\int \Delta p_r n_r dA$	$\int \Delta p_r n' dA$	$\int \Delta p' n_r dA$	$\int \Delta p' n' dA$
Fin-IF	C_T	0.64	0.64	0.43	-0.30	-0.12
	C_L (1/2 cycle)	1.28	1.96	-0.40	-0.38	0.10
Fin-HF	C_T	0.63	0.66	0.57	-0.40	-0.20
	C_L (1/2 cycle)	1.02	2.08	-0.62	-0.67	0.23

Table 1. Time-averaged decomposition of lateral force and thrust.

Discussion

Our results demonstrate that a flexible caudal fin generates efficient propulsion by the mechanism of local-force redirection. The alternative hypothetical mechanisms involving changes in pitching moments associated with pressure distributions (Fig. 2C, F) and changes in relative-phase between pressure, force, and velocity (Figs. 3B–C, 4B) do not substantially contribute to improved efficiency. Therefore, local-force redirection provides the solitary basis of mechanical intelligence by the caudal fin to generate efficient propulsion in fish swimming.

The efficiency gains provided by fin flexibility may be understood by considering the power requirements for propulsion. The power for each elemental area on the fin mesh (Fig. 1E) may be approximated by the product of its pressure difference (Δp) acting along the normal \hat{n} , area (dS) and velocity (V_{fin}). The total fin power at a given time may therefore be found by integrating this product over the area of the fin, i.e. $P(t) \approx \int_{S_{\text{fin}}} \Delta p \hat{n} V_{\text{fin}} dS$. This relationship underscores the crucial role of the timing of fin deformation (affecting the direction of \hat{n}) with respect to pressure and velocity changes.

During a tail-beat cycle, a fin undergoes significant variation in the net pressure differential across its surface (Fig. 3B). The extremes in pressure occur shortly after the mid-point of the stroke, coinciding roughly with the highest fin velocity (Fig. 3C), which serves as a multiplicative factor in generating power (Eqn. 1). The timing of fin deformation relative to the pressure differential (Fig. 4B,D) also further aids in improving the thrust performance of the flexible fins. In particular, extreme deformations in the fore-aft orientation roughly coincide with peak pressure to enhance thrust (Fig. 3B, G). Deformations in the dorso-ventral orientation proceed with similar timing (Fig. 3K) which serve to redirect lateral forces into directions that do not contribute to the power requirements (Eqn. 1). In fact, the lateral orientation of the most flexible fin is nearly minimal at these moments, which serves to reduce the generation of energetically costly lateral forces (Fig. 3C, H). Therefore, local-force redirection creates a matching of the timing of pressure and velocity changes in a manner that enhances propulsive efficiency. This seemingly complex juxtaposition of multiple physical occurrences that achieves efficient locomotion by leveraging physical interactions with the environment through the fin’s mechanical design. Facilitating this efficiency might otherwise be achieved through active sensing, neural integration, and muscular action. Bypassing these energetically expensive and potentially complex and less robust forms of control suggest that the flexible caudal fin offers a compelling example of mechanical intelligence.

These results address the Bainbridge conjecture on the benefits of fin flexibility (20). Upon observing the “billowing” of the caudal fin, Bainbridge suggested that the deformation of a flexible fin smooths out the variations in the thrust force generated by the fin for stable swimming motion. Our simulations show that while the peak-to-peak variations in thrust for these various fins are similar in magnitude (Fig. 4B), oscillations in the larger *lateral* force are lower for the flexible fins (Fig. 4C). This reduction in lateral force indeed tends to reduce the sway force, as well as yaw moment, induced by the fin to yield a smoother swimming motion. Therefore, the present FSI simulations support Bainbridge’s conjecture.

Propulsion with a flexible caudal fin bears similarities to the aerodynamics of wing deformations in flying animals. For example, these deformations improve the efficiency of flight in butterflies (30) and bluebottle flies (31). In addition, the flexibility of wings improves the lift generation during the clap-and-fling flight of butterflies (32). Thus, the current study offers an analogous example of how flexibility enhances propulsion in animal locomotion through the FSI dynamics.

The principle of local-force redirection for enhancing propulsive efficiency could be adopted in the design of efficient bioinspired propulsion systems. Such efficiency gains could enhance propulsion in autonomous underwater vehicles (33, 34), wave-assisted propulsion systems (35, 36), as well as flapping-foil based energy harvesting systems (37, 38).

Conclusion

The numerical simulations presented here demonstrate that flexible caudal fins significantly enhance the efficiency of propulsion by harnessing passive mechanical intelligence through local-force redirection. Flexible fins deform dynamically under fluid forces, effectively reorienting hydrodynamic pressures to optimize thrust production while minimizing energetically costly lateral forces. Unlike rigid fins, which experience greater lateral forces and increased power demands, flexible fins exploit dorso-ventral deformation to passively and continuously adjust their geometry to fluid dynamic conditions, resulting in efficiency gains of up to 70%. This form of mechanical intelligence highlights the potential for bioinspired designs that integrate compliant materials and structural flexibility to achieve improved energy efficiency and adaptability in engineered aquatic propulsion systems.

Materials and Methods

Fin Model. The caudal fin in the current study is assumed to have a canonical trapezoidal shape (Fig. 1E). The fin is comprised of stiff rays at the dorsal and ventral edges and these are joined together with an upstream edge of the fin, which represents the peduncle. The two rays and the peduncle form the frame of the fin and a flexible membrane capable of supporting extensional and bending stresses (technically, a “shell”) is stretched across this stiff frame. The frame is driven with a flapping motion given by

$$\theta(t) = \theta_0 \cos(2\pi ft); \quad A(t) = A_0 \sin(2\pi ft) \quad [3]$$

where $A(t)$ is the lateral (heaving) displacement of the fin peduncle, and $\theta(t)$ is the pitch angle of the fin at the peduncle. The membrane experiences hydrodynamic forces during the fin motion and this, combined with its inertia, drive the deformation of the fin. The key non-dimensional parameters are the pitch amplitude θ_0 , heave amplitude A_0/C (where C is the chord of the fin), Reynolds number ($\text{Re} = U_\infty C/\nu$) and Strouhal number ($\text{St} = 2A_0 f/U_\infty$). In the current study, we fix the values of θ_0 and A_0/C to 30° , 0.1, respectively. The pitch and heave amplitude are consistent with previous studies (24, 25, 39) and are a reasonable representation of the kinematics of the caudal fin of fish. Previous research on flapping wings and fins (40, 41) has shown that among the various non-dimensional parameters for such flows, the Strouhal number dominates the flow physics and if the Reynolds number is sufficiently high so that the boundary layers formed on the flapping control surface are thin compared to the overall movement of the control surface, the resulting flow physics will be a reasonable approximation to the flow at higher Reynolds number. In the current study, we fix the Reynolds number at a value of 1000 and ensure, through extensive grid refinement studies, that the flow is well resolved by the grid employed.

A. Flow Simulation. We perform the direct numerical simulations (DNS) of the flow by solving the incompressible Navier-Stokes equation described as:

$$\frac{\partial u_i}{\partial x_i} = 0; \quad \frac{\partial u_i}{\partial t} + \frac{\partial u_j u_i}{\partial x_j} = -\frac{\partial p}{\partial x_i} + \frac{1}{\text{Re}} \frac{\partial^2 u_i}{\partial x_j \partial x_j} \quad [4]$$

where u_i is the velocity and p is the pressure. The governing equations are discretized in space and time using the 2^{nd} -order finite-difference schemes and integrated in time using the operator splitting fractional step method. Here, the Eqn. 4 is split

B Membrane Dynamics Model and FSI Coupling

into the advection-diffusion (ADE) and pressure Poisson equation (PPE), and this results in two linear systems connected through an intermediate velocity. The linear system for ADE is solved using a line successive-over-relaxation solver, and the system for PPE is solved using a biconjugate-gradient stabilized solver. We utilize our in-house developed numerical solver ViCar3D (42) to implement the numerical schemes to perform calculations. The flow solver has been validated for a variety of fluid dynamics studies, including coupled FSI simulations (43–45), fish fins (46, 47), and flapping insect wings (48). The placement of the fin within the computational domain of size $26C \times 40C \times 40C$. A uniform grid is employed in a cuboidal region around the body to resolve the boundary layers and vortex structures, and the grid is stretched away outside this region to the outer boundary. We employ a grid resolution of $256 \times 256 \times 240$ (about 15 million points), which corresponds to about 100 points along the fin chord length. We have performed extensive grid refinement studies to ensure the simulations are grid converged. Each simulation is carried out for three flapping cycles, and the results for the 3rd cycle are used for all the analysis.

B. Membrane Dynamics Model and FSI Coupling. We utilize a connected spring-mass network model to simulate the hydro-elastic deformation in the elastic membrane. This class of model offers several computational advantages in studies with a focus on fluid dynamics. Moreover, the model is simple to couple with our sharp interface immersed boundary method. The fin surface is described by a mesh with triangular elements with the triangle vertices serving as “nodes” for the discretization of the dynamical equations. The structural dynamics is represented by the following ordinary differential equation Eq. (5).

$$M \frac{d^2 \mathbf{X}(t)}{dt^2} = \mathbf{F}_{\text{hydro}} - \mathbf{F}_{\text{elas}} - \zeta \frac{d \mathbf{X}(t)}{dt}, \quad [5]$$

In Eqn. 5, $M \in \mathbb{R}^{N \times N}$ is the diagonal matrix with nodal masses, $\mathbf{X}(t) \in \mathbb{R}^{N \times 3}$ contains the node positions in 3D space. $\mathbf{F}_{\text{hydro}}$ and $\mathbf{F}_{\text{elas}} \in \mathbb{R}^{N \times 3}$ are the hydrodynamic and elastic forces applied on the nodes, respectively. Material damping is modeled using the last term in Eqn. 5, with ζ being the structural damping coefficient. This method has been employed previously to model fluid-structural interaction of shells in a variety of applications (49–51) and we present a detailed description along with the validation of the model in our earlier work (52).

While the fin is geometrically represented as a zero-thickness membrane in the flow solver, the dynamical model of the membrane employs a finite thickness given in the above equations by $h^* = h/C$. This parameter appears in both the elastic and bending moduli and is therefore a convenient parameter for controlling the flexibility of the fin membrane. The non-dimensional material properties of the membrane are based nominally on the properties of animal tissue as follows: membrane (solid) to fluid density ratio $\rho^* (= \rho_s/\rho_f) = 1$; Elastic Modulus $E^* (= E/\rho U_\infty^2) = 10^6$; and the Poisson’s ratio $\nu = 0.4$. The damping coefficient C is unknown, and we chose an intermediate value of $\zeta (= C/2\sqrt{k_b m}) = 1$ which prevents excessive numerical oscillations in the membrane. Tests show that the overall results regarding thrust, power and efficiency are relatively insensitive to moderate variations in these properties.

C. Hydrodynamic Forces and Power Expenditure. The power expenditure of the fin is primarily associated with the work done by the fin against hydrodynamic forces. The hydrodynamic forces can be expressed as $\mathbf{F}_{\text{hydro}} = (\Delta p \hat{n}, \Delta \tau \hat{t}) dS$, where Δp and $\Delta \tau$ are the pressure and shear stress differentials across the fin surface, \hat{n} and \hat{t} are the unit vectors normal and tangential to the fin surface, and dS is an elemental area on the fin surface.

The thrust and lateral forces on the fin are obtained by integrating the x_1 and x_2 components of $\mathbf{F}_{\text{hydro}}$ over the fin surface. The power expended by the fin is dominated by the work done against the hydrodynamic forces and is given by $P = \int_{S_{\text{fin}}} \mathbf{F}_{\text{hydro}} \cdot \mathbf{V}_{\text{fin}} dS$. Given that at these high Reynolds numbers, $\Delta p \gg \Delta \tau$, the power expended by the fin can be approximated reasonably well as $P \approx \int_{S_{\text{fin}}} \Delta p \hat{n} \cdot \mathbf{V}_{\text{fin}} dS$. We use

C Hydrodynamic Forces and Power Expenditure

numerical integration over the fin surface to obtain the integral values associated with the hydrodynamic forces and power.

ACKNOWLEDGMENTS. SS, RM, and JHS acknowledge support from ONR Grants N00014-22-1-2655 monitored by Dr. Robert Brizzolara. MJM acknowledges ONR Grant N00014-19-1-2035

References.

1. SA Combes, TL Daniel, Flexural stiffness in insect wings: Scaling and the influence of wing venation. *J. Exp. Biol.* **206**, 2979–2987 (2003).
2. F Muijres, et al., Leading-edge vortex improves lift in slow-flying bats. *Science* **319**, 1250–1253 (2008).
3. RM Alexander, Energy-saving mechanisms in walking and running. *J. Exp. Biol.* **160**, 55–69 (1991).
4. DM Dudek, RJ Full, An isolated insect leg's passive recovery from dorso-ventral perturbations. *J. Exp. Biol.* **210**, 3209–3217 (2007).
5. DL Jindrich, RJ Full, Dynamic stabilization of rapid hexapedal locomotion. *J. Exp. Biol.* **205**, 2803–2823 (2002).
6. MA Daley, AA Biewener, Running over rough terrain reveals limb control for intrinsic stability. *Proc. Natl. Acad. Sci.* **103**, 15681–15686 (2006).
7. TJ Roberts, E Azizi, Flexible mechanisms: the diverse roles of biological springs in vertebrate movement. *J. experimental biology* **214**, 353–361 (2011).
8. A Gupta, S Savarese, S Ganguli, L Fei-Fei, Embodied intelligence via learning and evolution. *Nat. communications* **12**, 5721 (2021).
9. Z Zhao, et al., Exploring Embodied Intelligence in Soft Robotics: A Review. *Biomimetics* **9**, 248 (2024).
10. R Pfeifer, How the body shapes the way we think: A new view of intelligence (2006).
11. D Howard, et al., Evolving embodied intelligence from materials to machines. *Nat. Mach. Intell.* **1**, 12–19 (2019).
12. F Fish, GV Lauder, Passive and active flow control by swimming fishes and mammals. *Annu. Rev. Fluid Mech.* **38**, 193–224 (2006).
13. J Long, K Nipper, The importance of body stiffness in undulatory propulsion. *Am. Zool.* **36**, 678–694 (1996).
14. M Taguchi, JC Liao, Rainbow trout consume less oxygen in turbulence: the energetics of swimming behaviors at different speeds. *J. Exp. Biol.* **214**, 1428–1436 (2011).
15. JC Liao, Neuromuscular control of trout swimming in a vortex street: implications for energy economy during the Karman gait. *J. Exp. Biol.* **207**, 3495–3506 (2004).
16. DN Beal, FS Hover, MS Triantafyllou, JC Liao, GV Lauder, Passive propulsion in vortex wakes. *J. fluid mechanics* **549**, 385–402 (2006).
17. JC Liao, D Beal, GV Lauder, M Triantafyllou, Fish exploiting vortices decrease muscle activity. *Science* **302**, 1566–1569 (2003).
18. SJ Lighthill, *Mathematical biofluidynamics*. (SIAM), (1975).
19. JH Seo, R Mittal, Improved swimming performance in schooling fish via leading-edge vortex enhancement. *Bioinspiration & Biomimetics* **17**, 066020 (2022).
20. R Bainbridge, Caudal fin and body movement in the propulsion of some fish. *J. Exp. Biol.* **40**, 23–56 (1963).
21. GV Lauder, Function of the caudal fin during locomotion in fishes: kinematics, flow visualization, and evolutionary patterns. *Am. Zool.* **40**, 101–122 (2000).
22. BE Flammang, GV Lauder, Speed-dependent intrinsic caudal fin muscle recruitment during steady swimming in bluegill sunfish, *lepomis macrochirus*. *J. Exp. Biol.* **211**, 587–598 (2008).
23. AC Gibb, KA Dickson, GV Lauder, Tail kinematics of the chub mackerel *scomber japonicus*: testing the homocercal tail model of fish propulsion. *J. experimental biology* **202**, 2433–2447 (1999).
24. M Bergmann, A Iollo, R Mittal, Effect of caudal fin flexibility on the propulsive efficiency of a fish-like swimmer. *Bioinspiration & biomimetics* **9**, 046001 (2014).
25. D Fernández-Gutiérrez, WM Van Rees, Effect of leading-edge curvature actuation on flapping fin performance. *J. Fluid Mech.* **921**, A22 (2021).
26. MS Triantafyllou, G Triantafyllou, DK Yue, Hydrodynamics of fishlike swimming. *Annu. review fluid mechanics* **32**, 33–53 (2000).
27. J Rohr, et al., Observations of dolphin swimming speed and strouhal number. *Space Nav. Warf. Syst. Cent. Tech. Rep.* **1769** (1998).
28. GK Taylor, RL Nudds, ALR Thomas, Flying and swimming animals cruise at a Strouhal number tuned for high power efficiency. *Nature* **425**, 707–711 (2003).
29. GS Triantafyllou, MS Triantafyllou, MA Grosenbaugh, Optimal thrust development in oscillating foils with application to fish propulsion. *J. Fluids Struct.* **7**, 205–224 (1993).
30. L Zheng, TL Hedrick, R Mittal, Time-varying wing-twist improves aerodynamic efficiency of forward flight in butterflies. *PLOS ONE* **8**, 1–10 (2013).
31. SJ Hsu, H Deng, J Wang, H Dong, B Cheng, Wing deformation improves aerodynamic performance of forward flight of bluebottle flies flying in a flight mill. *J. Royal Soc. Interface* **21**, 20240076 (2024).
32. L Johansson, P Henningson, Butterflies fly using efficient propulsive clap mechanism owing to flexible wings. *J. Royal Soc. Interface* **18**, 20200854 (2021).
33. FE Fish, et al., Conceptual design for the construction of a biorobotic auv based on biological hydrodynamics in *13th International Symposium on Unmanned Untethered Submersible Technology*, Durham, NH, Aug. pp. 24–27 (2003).
34. MS Triantafyllou, AH Techet, FS Hover, Review of experimental work in biomimetic foils. *IEEE J. Ocean. Eng.* **29**, 585–594 (2004).
35. HS Raut, JH Seo, R Mittal, Hydrodynamic performance and scaling laws for a modelled wave-induced flapping-foil propulsor. *J. Fluid Mech.* **999**, A1 (2024).
36. HS Raut, JH Seo, R Mittal, Dynamics and thrust performance of a modeled multifoil wave-induced flapping foil propulsor. *Ocean. Eng.* **317**, 119930 (2025).
37. J Young, JC Lai, MF Platzer, A review of progress and challenges in flapping foil power generation. *Prog. Aerosp. Sci.* **67**, 2–28 (2014).
38. Q Xiao, Q Zhu, A review on flow energy harvesters based on flapping foils. *J. Fluids Struct.* **46**, 174–191 (2014).
39. H Dong, R Mittal, FM Najjar, Wake topology and hydrodynamic performance of low-aspect-ratio flapping foils. *J. Fluid Mech.* **566**, 309–343 (2006).
40. JM Anderson, K Streitlien, D Barrett, MS Triantafyllou, Oscillating foils of high propulsive efficiency. *J. Fluid mechanics* **360**, 41–72 (1998).
41. S Sekhar, P Windes, X Fan, DK Tafti, Canonical description of wing kinematics and dynamics for a straight flying insectivorous bat (*hipposideros pratti*). *PLoS One* **14**, e0218672 (2019).
42. R Mittal, et al., A versatile sharp interface immersed boundary method for incompressible flows with complex boundaries. *J. computational physics* **227**, 4825–4852 (2008).
43. K Shoele, R Mittal, Computational study of flow-induced vibration of a reed in a channel and effect on convective heat transfer. *Phys. Fluids* **26** (2014).
44. K Shoele, R Mittal, Flutter instability of a thin flexible plate in a channel. *J. Fluid Mech.* **786**, 29–46 (2016).
45. S Bailoor, JH Seo, LP Dasi, S Schena, R Mittal, A computational study of the hemodynamics of bioprosthetic aortic valves with reduced leaflet motion. *J. Biomech.* **120**, 110350 (2021).
46. H Dong, M Bozkurtas, R Mittal, P Madden, GV lauder, Computational modelling and analysis of the hydrodynamics of a highly deformable fish pectoral fin. *J. Fluid Mech.* **645**, 345–373 (2010).
47. J Zhou, JH Seo, R Mittal, Hydrodynamically beneficial school configurations in carangiform swimmers: Insights from a flow-physics informed model. *arXiv preprint arXiv:2501.09299* (2025).
48. L Zheng, TL Hedrick, R Mittal, A multi-fidelity modelling approach for evaluation and optimization of wing stroke aerodynamics in flapping flight. *J. Fluid Mech.* **721**, 118–154 (2013).
49. MD de Tullio, G Pascazio, A moving-least-squares immersed boundary method for simulating the fluid–structure interaction of elastic bodies with arbitrary thickness. *J. Comput. Phys.* **325**, 201–225 (2016).
50. DA Fedosov, B Caswell, GE Karniadakis, Systematic coarse-graining of spectrin-level red blood cell models. *Comput. Methods Appl. Mech. Eng.* **199**, 1937–1948 (2010).
51. V Spandan, et al., A parallel interaction potential approach coupled with the immersed boundary method for fully resolved simulations of deformable interfaces and membranes. *J. computational physics* **348**, 567–590 (2017).
52. S Kumar, JH Seo, R Mittal, Computational modeling and analysis of the coupled aero structural dynamics in bat inspired wings. *arXiv preprint arXiv:2501.02034* (2025).